PHYSICAL REVIEW B **97**, 024418 (2018)

Editors' Suggestion

Origin of the net magnetic moment in $LaCoO_3$

G. M. Kaminsky,[1] D. P. Belanger,[1] F. Ye,[2] J. A. Fernandez-Baca,[2] J. Wang,[2,3] M. Matsuda,[2] and J.-Q. Yan[4]
[1]*Department of Physics, University of California, Santa Cruz, California 95064, USA*
[2]*Neutron Scattering Division, Oak Ridge National Laboratory, Oak Ridge, Tennessee 37831, USA*
[3]*Department of Physics, Renmin University of China, Beijing 100872, China*
[4]*Material Science and Technology Division, Oak Ridge National Laboratory, Oak Ridge, Tennessee 37831, USA*

(Received 30 June 2017; revised manuscript received 1 December 2017; published 19 January 2018)

We use polarized neutron scattering to characterize the Bragg scattering intensity below $T_C = 89.5$ K at the (1,0,0) pseudocubic nuclear Bragg point of $LaCoO_3$. Upon cooling in a field (FC), a net magnetic moment is apparent in Bragg scattering intensity, just as it was in previous magnetization measurements. Critical behavior associated with the net moment near T_C upon cooling in small applied fields rapidly rounds with increasing field strength. We show, using a mean-field calculation, that this net moment can develop in a metastable state that forms upon FC, even when all the interactions in the system are antiferromagnetic.

DOI: 10.1103/PhysRevB.97.024418

I. INTRODUCTION

The unusual magnetic behavior of bulk $LaCoO_3$ (LCO) below $T = 100$ K is well known but has not been well understood microscopically. Magnetization measurements clearly show that the dominant interaction between spins is antiferromagnetic for $T > 100$ K, but the system does not attain long-range order at low T [1–3]. The antiferromagnetic short-range correlations grow as T decreases until $T_o \approx 37$ K, below which antiferromagnetic correlations rapidly decrease [1,3,4]. Each Co ion is surrounded by an octahedron of six oxygen atoms, with each oxygen being shared with an adjacent octahedron that is rotated by the Co-O-Co bond angle γ. In the bulk, far from surfaces and defects, γ decreases as T decreases, reaching $\gamma_C \approx 163^\circ$ at T_o. For $\gamma < \gamma_C$, the bonds between adjacent Co are nonmagnetic, whereas bonds for which γ is a few degrees larger than γ_C are strongly antiferromagnetic [1,5]. Despite the collapse of antiferromagnetic interactions, in small applied fields, $H < 100$ Oe, a small net moment exhibits sharp, critical-like behavior near $T_c = 89.5$ K; the rounding of the transition is unusually rapid as the field is increased [1,2,6]. Near surfaces and defects [2,7], the average γ remains larger than γ_C. What has not been well understood microscopically is how a dominantly antiferromagnetic system that does not achieve antiferromagnetic long-range order nevertheless generates a net moment that persists to low T and why the critical-like behavior associated with it rounds rapidly with increasing applied fields.

In an earlier paper, Yan *et al.* [6] studied the net moment in bulk LCO crystals. Although the precise mechanism generating the net moment could not be established, it was shown that it increased with increasing crystal surface area. In other studies [7], particles with diameters of 30 to 1000 nm diameter were grown and it was shown that impurity phases greatly enhance the net moment over that observed in bulk crystals. Surprisingly, high quality bulk crystals, which have negligible impurity phase defects and a relatively small surface area per volume, nevertheless exhibit a small net magnetic moment in magnetization measurements done while cooling in an applied field (FC) [1,3,6]. A different state is entered when cooled to low temperature, the field is applied, and the temperature is raised (ZFC). In the magnetization measurements, only when the applied field is extremely small, $H < 3$ Oe, the net moment is largely suppressed. It is not clear from the experiments whether the FC or ZFC procedure results in a state closer to the ground state.

The oxygen octahedral rotations provide a basis for modeling the magnetic ordering that produces a net moment near T_C for small H. As shown below, polarized neutron scattering measurements in large, high-quality LCO crystals indicate a magnetic transition at T_C with scattering at the pseudocubic (1 0 0), indicating the same periodicity as the underlying lattice. The number of spins near the crystal surfaces in this case should be negligible; clearly, neither the surface nor impurity defects are plausible sources of the observed moment. LCO is generally accepted to have $R\bar{3}c$ symmetry with a nuclear reflection at hexagonal (1 0 −2), though one early study [8] suggested a lower $I2/a$ symmetry, perhaps being indicative of small strains in the system. Twinning is ubiquitous in this structure, so in experiments it is more convenient to use the pseudocubic notation where, for example, (1 0 0) corresponds to the hexagonal (1 0 −2) reflection. We will use the pseudocubic notation in our discussions. The scattering appears at four points around the (1 0 0) Bragg point corresponding to the four orientations of the twin domains, but the measurements integrate over two peaks in the vertical direction, which has a wide resolution. We argue below that much of the net moment could originate at twin interfaces. Both (1 0 0) and (1 1 0) pseudocubic twin planes tend to occur, but (1 0 0) twins are predominant [9,10]. Modeling γ for bonds across the interface indicates a pattern where half the bonds are greater than γ_C and, hence, strongly antiferromagnetic, and alternate with nonmagnetic bonds with $\gamma < \gamma_C$. This alternating pattern breaks the symmetry between the antiferromagnetic sublattices. We use a mean-field model incorporating that asymmetry to show how antiferromagnetic

2469-9950/2018/97(2)/024418(13)

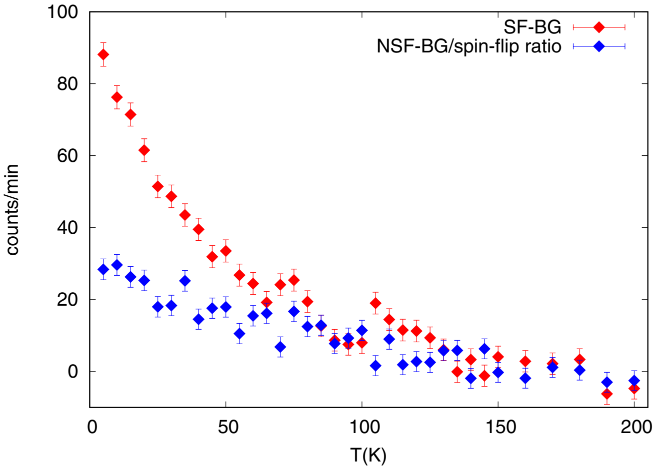

FIG. 1. Polarized neutron intensity of the (1 0 0) pseudocubic Bragg scattering vs T for both the spin-flip (SF) and non-spin-flip (NSF) configurations after subtracting the background (BG) determined from fits for $145 < T < 200$ K, as described in the main text. The counting times for the SF and NSF data were 45 and 5 minutes, respectively.

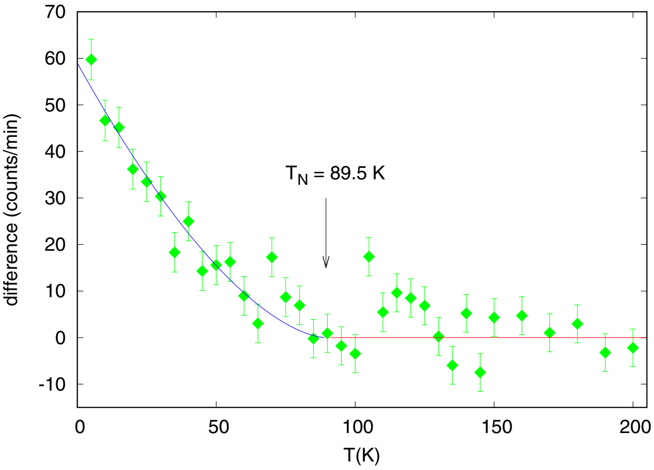

FIG. 2. The difference between the SF and NSF intensities vs T, The NSF intensity is normalized by the spin-flip ratio of 9.8 and both the SF and NSF intensities had backgrounds subtracted as described in Fig. 1. The curve represents Eq. 1 with $T_C = 89.5$ K, $A = 59.0$, $\beta = 0.88$, $B = 0$, and $C = 0$.

ordering at (1 0 0) twin interfaces can generate net metastable moments that mimic the behaviors observed in experiments.

II. NEUTRON SCATTERING RESULTS

Polarized neutron scattering experiments were performed on two LCO single crystals using the triple axis spectrometer HB1 at the High Flux Isotope Reactor. For the results shown in Figs. 1 and 2, obtained with crystal A that has the approximate dimensions of 4 mm in diameter and 8 mm in length, the neutron energy was 13.5 meV and the energy resolution was 1.3 meV using a collimation configuration of 48’, 80’, 80’, and 240’. Heusler crystals were used for the monochromator and analyzer and a flipping ratio, the ratio of up spins to down spins in the polarized beam, of 9.8 was achieved [11]. The polarized neutron experiment has a spin-flip (SF) configuration to determine the intensity of magnetically scattered neutrons and a non-spin-flip (NSF) for neutrons scattered from the coherent nuclear scattering, where the polarization direction is aligned with the scattering vector $\vec{Q}$. The spin flipping ratio is a measure of the mixing of these resulting due to the imperfect beam polarization. For the measurements using crystal A, the SF and NSF intensities were measured with the neutron spin aligned along $\vec{Q}$. A closed-cycle refrigerator was employed in measuring the T dependence of the SF and NSF intensities for $4 < T < 300$ K. Because the field at the sample was 16 to 18 Oe throughout the experiment, all data were taken under FC conditions. The $LaCoO_3$ single crystals for these results was grown by the floating zone technique using an optical image furnace as reported elsewhere [12].

The polarized neutron technique discriminates against nuclear Bragg scattering, which would otherwise obscure the small magnetic contribution [11]. Figure 1 shows data collected in both the SF and NSF configurations using crystal A. The NSF intensity is divided by the flipping ratio. A background contribution (BG), determined by averaging the data for $145 < T < 200$ K, is subtracted from each data set. The SF configuration clearly shows a small, but significant magnetic Bragg scattering contribution. The difference of the two sets of data is plotted in Fig. 2. Using the difference, we can characterize the critical behavior associated with the phase transition to long-range order by fitting to

$$I = At^{2\beta} + B + Ct, \tag{1}$$

where $t = (T_C - T)/T_C$ and A is nonzero only for $t > 0$. T_C is set to 89.5 K, the value obtained in magnetization experiments [2]. A fit with $B = 0$ and $C = 0$ yields $A = 59.0 \pm 4.8$ and $\beta = 0.82 \pm 0.11$, where the error estimates reflect only the statistical error of the fit. The critical exponent β obtained from magnetization measurements [1,2] on bulk LCO particles is $\beta = 0.63 \pm 0.02$. Including a linear background term in the fit yields $A = 58.6 \pm 4.9$, $\beta = 0.97 \pm 0.14$, and $C = 2.9 \pm 1.2$. If, instead, a T-dependent term BT is included, we obtain $A = 60.3 \pm 5.2$, $\beta = 0.80 \pm 0.11$, and $B = -1.5 \pm 2.1$. Neither of the latter two fits improves the quality of the fit significantly over the one with $B = 0$ and $C = 0$. The error estimates are statistical fit errors; they do not reflect systematic errors. The transition temperature is taken from magnetometry measurements and its value is one source of systematic error. The value of β is not determined as accurately as in the magnetometry experiments, but both experiments are consistent with $\beta > 1/2$. Normally, one expects $\beta \lessapprox 1/3$ for 2D or 3D transitions, but $\beta > 1/2$ is consistent with bulk-assisted surface critical behavior [2,13,14] and is consistent with ordering taking place at twinning interfaces. The bulk-assisted surface ordering exponent $\beta \approx 0.75$ [2,14] results from the surface ordering with different critical behavior from the bulk. Two apparent differences between LCO and the surface-ordering models are that bulk LCO does not order sufficiently far from surfaces and we observe a net moment, which might seem inconsistent with the antiferromagnetic order parameter of the bulk. However, antiferromagnetic moments away from the surfaces are close to ordering while those near the surface do order [7], and we

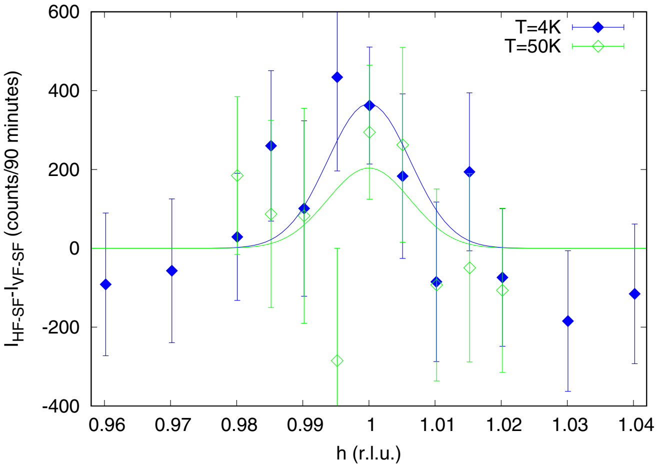

FIG. 3. The (h 0 0) magnetic scattering intensity at $T = 4$ and 50 K for crystal B, obtained by subtracting the intensity with the neutron polarization perpendicular to $\vec{Q}$ ($I_{\text{VF-SF}}$), which is in the vertical to the scattering plane, from the intensity with the polarization parallel to $\vec{Q}$ ($I_{\text{HF-SF}}$). The curves are fits with the background set to zero and with $A = 248$ and 186 counts per 90 minutes for $T = 4$ and 50 K, respectively, using the HWHM of 0.0075 r.l.u. determined from the (1 0 0) nuclear scattering peak.

will argue that, despite the net moment being generated, the ordering is essentially antiferromagnetic. With the ordering of the bulk and surface being antiferromagnetic, the situation in LCO is analogous to the surface-ordering model.

Depolarization of the beam in ordered ferromagnets can contribute to the temperature dependence of the SF signal if they have internally well-ordered domains that are misaligned with respect to each other. This should not be an issue for this antiferromagnetic system because the scattering is only from the weak net moment at twin interfaces. We can verify that depolarization effects are not important in these measurements by determining that the flipping ratio at the nuclear peak (2 0 0) is nearly T independent. We used crystal B, grown in the same manner as crystal A, but with dimension 0.5 cm in diameter and 2.5 cm in length. The flipping ratio is $10.56^{+0.09}_{-0.08}$ at $T = 295$ K and $10.41^{+0.08}_{-0.09}$ at $T = 4$ K, indicating no significant change with T.

The neutron scattering from the net moment is only from components perpendicular to $\vec{Q}$. To isolate the magnetic contribution in a way that is independent of all nonmagnetic influences, we measured the SF intensity with the neutron spin polarization parallel to $\vec{Q}$ and perpendicular to it [11]. For the polarization parallel to $\vec{Q}$, the SF intensity picks up all contributions perpendicular to $\vec{Q}$. For the polarization perpendicular to $\vec{Q}$, only magnetic contributions perpendicular to both $\vec{Q}$ and the polarization direction are observed. The nonmagnetic background should be essentially identical in the two geometries and the difference should only be magnetic scattering.

Figure 3 shows the resulting magnetic scattering intensity in a (h 0 0) scan obtained from the subtraction of the intensities of the two geometries at $T = 4$ and 50 K. Because the magnetic scattering is weak, long counting times between 60 and 120 minutes were used for each point. The resolution widths, determined from Gaussian fits to the (1 0 0) nuclear scattering peaks, are 0.0075(2) r.l.u. in the longitudinal direction and 0.0035(3) r.l.u. in the transverse direction. Fitting the longitudinal magnetic peak with a Gaussian line shape plus a constant background using the HWHM of 0.0075 r.l.u. and setting the backgrounds to zero, we obtain the Gaussian amplitude 367 ± 104 and 203 ± 117 at 4 and 50 K, respectively. If we let the background vary, we obtain the amplitude 323 ± 113 and background 34 ± 35 at $T = 4$ K and the amplitude 90 ± 46 and background 93 ± 47 at $T = 50$ K. For $T = 4$ K, the intensity at $h = 1$ is clearly dominated by a near-resolution magnetic Bragg component. At $T = 50$ K, the intensity at $h = 1$ could be partly from a very small Bragg component and partly from a broad paramagnetic scattering component; the relative importance is not clear from the data. Similar measurements in the transverse direction were inconclusive for both $T = 4$ and 50 K. The lack of a resolution-limited peak evident in the transverse scan possibly indicates that there is a small spread in the orientation angle of the twin planes. In experiments with larger energies (41 meV) to enhance scattering from fluctuations [15], it was observed that paramagnetic scattering decreases rapidly with decreasing temperature near $T = 50$ K. It was shown that paramagnetic scattering is relatively small at for lower energies such as the energy 13.5 meV used in our experiments. However, with small scattering intensities from the net moment, there could be a small effect. Excitations in LCO have been observed [16,17] in LCO near 50 K and could contribute to a small $\vec{Q}$-independent background. If a small broad paramagnetic background does play a role in the results shown in Fig. 2, it is to add to the intensity measured at the Bragg point, particularly at $T = 50$ K, and the effect would be to decrease the effective value determined for β; it would not change the conclusion that $\beta > 1/2$.

Although the magnetometry and neutron scattering results yielding $\beta > 1/2$ indicate critical behavior from 2D interfaces, the Bragg scattering is expected to be at 3D Bragg scattering points. For a case where the net moment on parallel interfaces is uncorrelated, the 2D behavior caused by the restriction of the growth of the fluctuation correlation length in the direction perpendicular to the interfaces would result in scattering rods, also perpendicular to the interfaces. This can be seen, for example, in 2D layered antiferromagnets that have extremely small interactions between planes [18]. In the case of LCO, the net moments on the parallel interfaces are highly correlated; the net moment on each plane is in the same direction determined by the applied field, and the planes are spaced an integer number of lattice spacings from all similar planes. The planes interfere constructively to create scattering at 3D points. The critical behavior is 2D, but the scattering structure is 3D.

Because the scattering from the net moment appears at the 3D pseudocubic scattering point, we know that the spatial periodicity of the net moment matches the underlying Co ion lattice. Using this result, we introduce in the following sections a model to explain how a net moment can form in LCO at the twin interfaces even in the case where all interactions are antiferromagnetic. The model is for one twin interface, but can be applied to LCO where there are many such interfaces with various orientations resulting from the twinning. Although the field is chosen to be along one of the octahedral axes (or average octahedral axis direction in the case

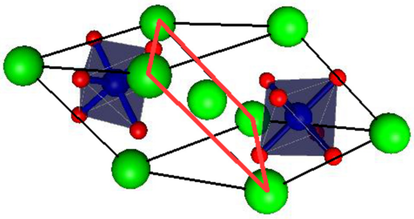

FIG. 4. The primitive rhombohedral LCO cell showing La ions (green) at the center and corners and two Co ions (blue) along with their oxygen octahedra. The rhombohedron is elongated along the line containing the two Co ions. The red lines connecting four La ions represents one of three possible twinning planes in the pseudocubic representation, each one containing four La ions at the rhombohedron corners and the central La ion, but no Co ions.

of tilted octahedra) to simplify the calculations, the field at any particular interface can be treated as having components along each octahedral axis and the model can be applied to each. A specific direction of neutron spin polarization is not a part of the model, but for each interface it will have components along the different octahedral axes. The various components of field and polarization directions in an LCO experiment can be modeled and superposition of the results allows the model to be applied to the scattering and magnetometry experimental results without loss of generality.

III. GEOMETRIC INTERFACE MODEL

The behavior of LCO magnetism well away from twin interfaces and other defects has been fairly well characterized. Experiments [1–3,7] and calculations [5] indicate that antiferromagnetic correlations are supported only for γ greater than the critical value $\gamma_C \approx 163^\circ$. The uniqueness of bulk LCO magnetism derives from the average value of γ decreasing with T to γ_C at T_o. The magnetic structure at twin boundaries is more complicated than that of the bulk far from the interface and can lead to antiferromagnetic ordering with a net moment along H_z. We first show how the interface can lead to a magnetic bond structure that is asymmetric with respect to the two antiferromagnetic sublattices.

The most common LCO twin interface in LCO is at a (1 0 0) pseudocubic plane [9,19]. Although other twin representations are possible, they are relatively uncommon, so we use the (1 0 0) one to model the possible consequences of a twin plane in LCO. A (1 0 0) plane can be visualized in the unit cell shown in Fig. 4 as a plane containing the central La ion, four other La ions, and no Co ions. There are four unique crystallite orientations possible associated with mirror reflections about the three (1 0 0) planes. Although the oxygen atomic positions are not distorted on the twin plane itself, the crystalline planes on either side are slightly misaligned with respect to each other. In our model, we locate the twin interface on an oxygen plane because that allows the oxygen octahedra to remain undistorted; only the angles between them change. The misalignment of crystal structures on either side of a twin plane is illustrated in Fig. 5, where, in the upper figure, a chain of Co ions in each of the crystals is shown nearly perpendicular to the twin interface located at the center where the bicolored oxygen is shared by both chains. In the lower figure, the chain of crystal on the left is extended into the crystal on the right to illustrate the misalignment. An important consequence of the misalignment is that the Co-O-Co bonds across the twin plane deviate from angles near the critical angle $\gamma_C \approx 163^\circ$ that exist for all other bonds. Half the bonds spanning the twin interface have $\gamma \approx 165^\circ$ and are adjacent to the other half that have $\gamma \approx 161^\circ$.

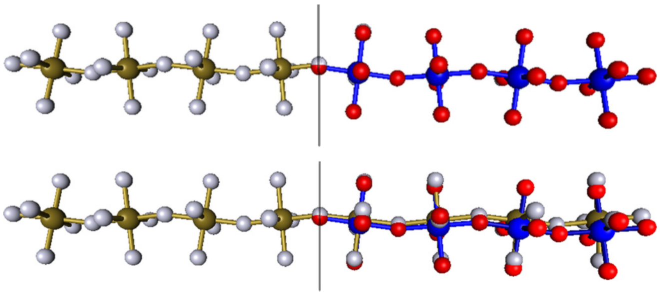

FIG. 5. A chain of Co ions crossing a twin interface, represented by the vertical line at the center. The upper figure shows blue ions representing a chain of Co ions that is nearly perpendicular to the twin plane in a crystallite to the right of the twin plane. Each Co is in the center of an oxygen octahedron (red). The gold-colored Co ions, surrounded by their oxygen octahedra (white), are from the crystallite to the left of the twin interface. The bi-colored oxygen is on the twin interface and is shared by both chains. The lower figure is the same as the upper one except that the chain from the left is extended into the right crystallite to emphasize the small misalignment of the two chains. The Co-O-Co angles are near 163° except across the twin interface, where half the bond angles are near 165° and half near 161°, in an alternating pattern.

Based on studies of LCO nanoparticles [7] and thin films [19–23], bond angles with $\gamma \approx 165^\circ$ should be strongly magnetic, much more so than in bulk LCO, whereas $\gamma \approx 161^\circ$ would result in essentially nonmagnetic bonds [1,3,5]. First-principles generalized gradient approximation (GGA) and local density approximation (LDA) [5] suggest the same dependence of the magnetization on γ; greater rhombohedral distortions corresponds to smaller values for γ and that suppresses the magnetic moment. The alternating pattern of strongly magnetic and nonmagnetic bonds across the twin interface is depicted in Fig. 6, which shows the Co and O ions in one plane adjacent to the twin interface and Fig. 7, which shows the bonds across the interface. The alternating configuration of bond strengths will affect the two antiferromagnetic sublattices asymmetrically. All Co-O-Co bonds not spanning the twin interface remain near the normal bulk angles close to 163°, with correspondingly weak antiferromagnetic interactions that are insufficient to cause long-range order on their own. In the actual LCO system, the distortions could propagate further than one Co plane from the twin interface, but that would likely not alter the physical behavior qualitatively.

The neutron scattering experiment has established that the ordering of the net moment has the spatial periodicity of the underlying lattice. The scattering is likely associated with the ordering of moments at the twinning interfaces and we will model below the consequences of the bond angle modifications across the interfaces. The modeling will assume that the only

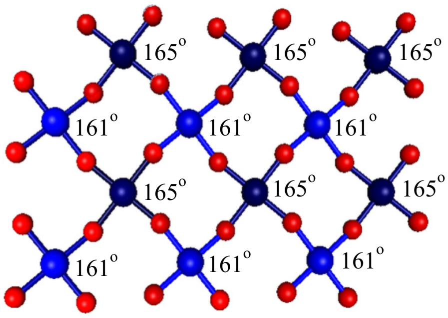

FIG. 6. The pattern of ions in one plane adjacent to the twin interface with strongly antiferromagnetic bonds across the interface (dark) alternating ions with nonmagnetic bonds (light) across the interface. The angles associated with the bonds across the interface (perpendicular to the page, but not shown) are next to the associated Co ions. All bond angles in the plane shown are 163°, as are all other angles for bonds that do not traverse the twin interface. Note that in the LCO crystal, multiple orientations of the interface exist because of the possible twins throughout the crystal.

anisotropy is the cubic anisotropy introduced by the oxygen octahedra. In that approximation, the orientation of the field to the interface is not important. The model calculation is for a field along any of the octahedral axes, except in the case of tilted octahedra. For a field along a general direction, we can apply the model to the components of the field along each of the octahedral axes.

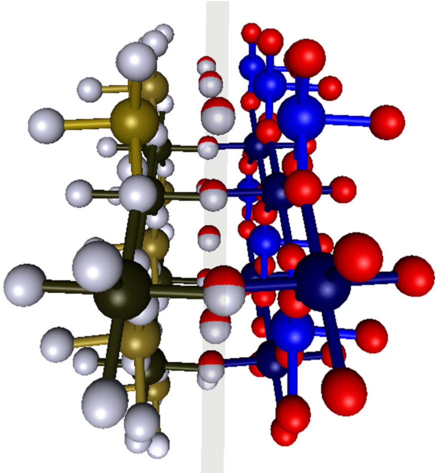

FIG. 7. A side view of the twin interface where only the strong antiferromagnetic bonds are shown spanning the interface (shown in the shaded region). The nonmagnetic bonds are not shown. The La ions are also not shown for clarity, including those that lie on the twin boundary. The two planes of Co ions are parallel. The bicolored oxygens are on the twin interface and are shared by oxygen octahedra from each of the two twin domains. Because of the twinning in LCO, such interfaces will be oriented in various directions and any field applied to the LCO crystal will, in general, have varying components along different octahedral axes.

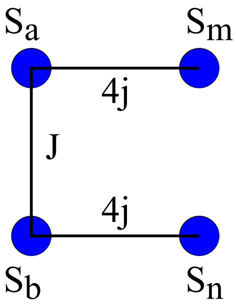

FIG. 8. Mean-field exchange interactions. S_a and S_m are on one side of the twin interface and S_b and S_n are on the other. The S_a and S_m each have four neighbors, each with interaction strength j. S_a and S_b interact with strength J and S_m and S_n do not directly interact with each other.

IV. GROUND-STATE CALCULATION

To explore the magnetic consequences of the pattern of alternating strongly antiferromagnetic and nonmagnetic bonds, we approximate the system by interacting classical local moments located at each Co ion site in the two planes adjacent to the twin interface. The strong magnetic interactions of strength J across the interface alternate with bonds of zero strength, as shown in Figs. 6 and 7. The moments away from the interface, which do not order in LCO but still contribute to the ordering at the twin interface, are represented in the model by an effective interaction j between all Co ions within each Co plane. Note that $J > j$ in our model because a stronger magnetic interaction is expected for the larger Co-O-Co bond angle [1,5]. In the ground-state calculations, each of the four kinds of spin, S_a, S_b, S_m, and S_n, behave like the others of the same kind. Hence the magnetic exchange interaction structure of this simple model is shown in Fig. 8 and is represented by a simplified magnetic model Hamiltonian with a magnetic field of strength H_z in the z direction,

$$\begin{aligned}\mathcal{H} = {} & 4j\vec{S_a}\cdot\vec{S_m} + 4j\vec{S_b}\cdot\vec{S_n} + J\vec{S_a}\cdot\vec{S_b} \\ & - H_z(S_{az} + S_{bz} + S_{mz} + S_{nz}) \\ & + F\left(\sum_{i\in x,y,z}\left[S_{a,i}^4 + S_{b,i}^4 + S_{m,i}^4 + S_{n,i}^4\right]\right).\end{aligned} \tag{2}$$

Because the interactions between spins are isotropic, no particular octahedral axis is favored with respect to the orientation of the twin interface. The field is applied in the z direction, along one octahedral axis, without loss of generality. In an experiment on LCO, the orientation of twin interfaces varies throughout the crystal, but the model can be applied to each component along the different octahedral axes and the solutions can be superimposed. The magnitude of each moment is constrained by $|S_i| = 1$ for $i \in a,b,m,n$. The S_a and S_b spins interact with magnitude J across the interface, and there are four interactions of strength j between S_a and S_m in the plane on one side of the interface and, likewise, four between S_b and S_n in the plane on the other side of the interface, as shown in Fig. 8. There are no direct interactions between S_m and S_n or between spins in the two planes and spins further from the interface. Local moments on each cobalt site

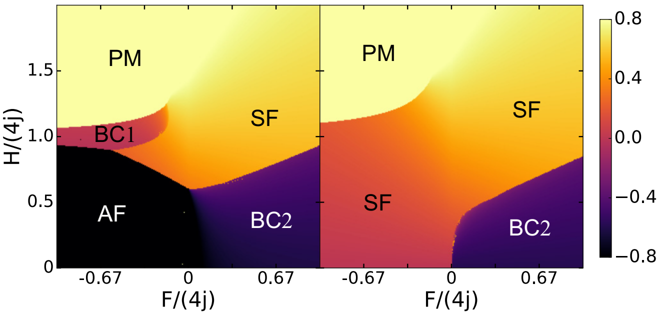

FIG. 9. The ground-state maps for $J = 0$, with $\Delta = 0.8$ (left) and 1.0 (right). The case $\Delta = 0.8$ agrees well with previous studies [24,25] and the case $\Delta = 1.0$ is isotropic, as in the model developed for the LCO twin interface. For $\Delta = 0.8$, both the antiferromagnetic (AF) state with moments along H and the biconical states (BC1 and BC2) are clearly visible, as is the paramagnetic (PM) state that appears at high fields. For $\Delta = 1.0$, the antiferromagnetic state is absent, as is expected.

also interact with the oxygens in the corners of the octahedra. To model this behavior, we introduce a cubic anisotropy into the model of strength F. Moments are attracted to the corners of the octahedra for $F < 0$ and repelled for $F > 0$. Similar models with quartic terms in the Hamiltonian were investigated previously by other groups [24–26].

We investigate the ground state by minimizing the energy represented by the Hamiltonian. Details of the procedure are described in Appendix. We tested it on a simple Heisenberg model with uniaxial exchange anisotropy and cubic anisotropy represented by

$$\begin{aligned}\mathcal{H} = {} & 4j[\Delta(S_{a,x}S_{m,x} + S_{a,y}S_{m,y}) + S_{a,z}S_{m,z}] \\ & - H_z(S_{az} + S_{mz}) + F\sum_{i\in x,y,z}\left[S_{a,i}^4 + S_{m,i}^4\right],\end{aligned} \tag{3}$$

where $\Delta < 1$ represents uniaxial anisotropy. The left panel of Fig. 9 shows our simulation results with $\Delta = 0.8$ for the net moment along H_z as a function of H_z and F. Such a model has been studied previously [24,25], and the results are essentially the same as ours; the only significant difference is that the boundary between the biconical BC2 and paramagnetic (PM) phases is flatter in the previous simulations. The antiferromagnetic state is visible for low H and $F < 0$. Higher fields result in the formation of a biconical state, BC1 [24,25], in which one spin points towards the corner of the oxygen octahedron in the direction of H_z, and the other spin remains near the $x-y$ plane, pointing towards one of octahedral corners. The angle between the spins is close to 90°. As the magnitude of H_z increases, the system becomes paramagnetic. For $F > 0$ and small H_z, a biconical BC2 state occurs as spins avoid the octahedral corners and instead tend to point towards the octahedral diagonals.

The right panel of Fig. 9 shows results for $\Delta = 1$, which represents isotropic exchange interactions and corresponds to the model in Eq. (2) for $J = 0$, which creates two identical noninteracting planes, only one of which is shown in the figure. For $F < 0$ and small H_z, the ground state is a spin-flop configuration (SF) with the moments aligned mostly perpendicular to the applied field with a small component induced along the field. For larger fields, the system becomes paramagnetic with a significant moment along H_z. For $F > 0$, the low field biconical BC2 state is observed. It gives way to a spin-flop state (SF) at higher fields.

The mean-field calculations ignore fluctuations. However, for $\Delta = 1$, density matrix renormalization group (DMRG) calculations in 1D [26], for which fluctuations are maximized, yield results qualitatively similar to those of the analogous mean-field calculations.

Simulations with $J \neq 0$ were done as well. Figure 10 shows the ground-state diagram for Eq. (2) with $j = 15$ and $J/(4j) = 2/3$. We use the value $J/(4j) = 2/3$ throughout this discussion, but the results were found to be qualitatively similar for simulations with $J/(4j) = 1/3$ and $4/3$. For $F \leqslant 0$, the ground state is a SF configuration with the moments predominantly perpendicular to H_z with small components along H_z. This can be seen in Fig. 10, which shows cuts of the grounds state diagram at $F/(4j) = -0.67$, 0, 0.67. In the lower part of Fig. 10, the moments on the left are along the field and those on the right are perpendicular to the field; for example, the label S_{axy} signifies the total perpendicular moment $\sqrt{S_{ax}^2 + S_{ay}^2}$. (The same notation is used for Figs. 11 and 12.) For $F > 0$, a biconical BC2 state is observed at small H, as shown in Fig. 10. As H_z increases, the system evolves towards SF, with an intermediate phase separating the two. The nature of BC1 and BC2 state can be seen from the cuts at $F/(4j) = -0.67$, 0 and 0.67. The BC1 state visible for $F < 0$ and the BC2 state is visible for $F > 0$.

Although there is no compelling model where $\gamma = 165°$ corresponds to a dominant ferromagnetic interaction between S_a and S_b, we investigated the consequences of $J < 0$ in the mean-field approximation. Figure 11 shows the ground-state diagram for $J/(4j) = -2/3$ and cuts at $F/(4j) = -0.67$, $F = 0$, and $F = 0.67$. For $F \leqslant 0$, the ground state is a SF configuration with the moments predominantly perpendicular with a small component along the field. The main difference between this case and that of $J/(4j) = 2/3$ is the orientation of S_a and S_b spins, which now always align in the same direction. For $F < 0$, the BC1 state is absent and the SF state transitions directly into the PM state with increasing H. This is expected because the interaction between S_a and S_b is ferromagnetic. For $F > 0$ a biconical BC2 state remains. It differs from the case for $J < 0$ in that the two moments S_a and S_b are aligned in the same direction, as are the two moments S_m and S_n.

Finally, we introduce the tilt of the octahedron into the simulation. As shown in Figs. 5–7, each Co-O-Co bond angle is 165°, so each oxygen octahedron is tilted relative to its neighbors, in an alternating pattern. The ground state is calculated using the modified equation

$$\begin{aligned}\mathcal{H} = {} & 4j\vec{S_a}\cdot\vec{S_m} + 4j\vec{S_b}\cdot\vec{S_n} + J\vec{S_a}\cdot\vec{S_b} \\ & - H_z(S_{az} + S_{bz} + S_{mz} + S_{nz}) \\ & + F\sum_{i\in x,y,z}\left(\sum_{k\in a,n}[\mathbf{M_1}\vec{S_k}]_i^4\right) + F\sum_{i\in x,y,z}\left(\sum_{k\in b,m}[\mathbf{M_2}\vec{S_k}]_i^4\right),\end{aligned} \tag{4}$$

where $\mathbf{M_1}$ and $\mathbf{M_2}$ are matrices that rotate spins into the coordinate systems of respective octahedra tilted 7.5° and

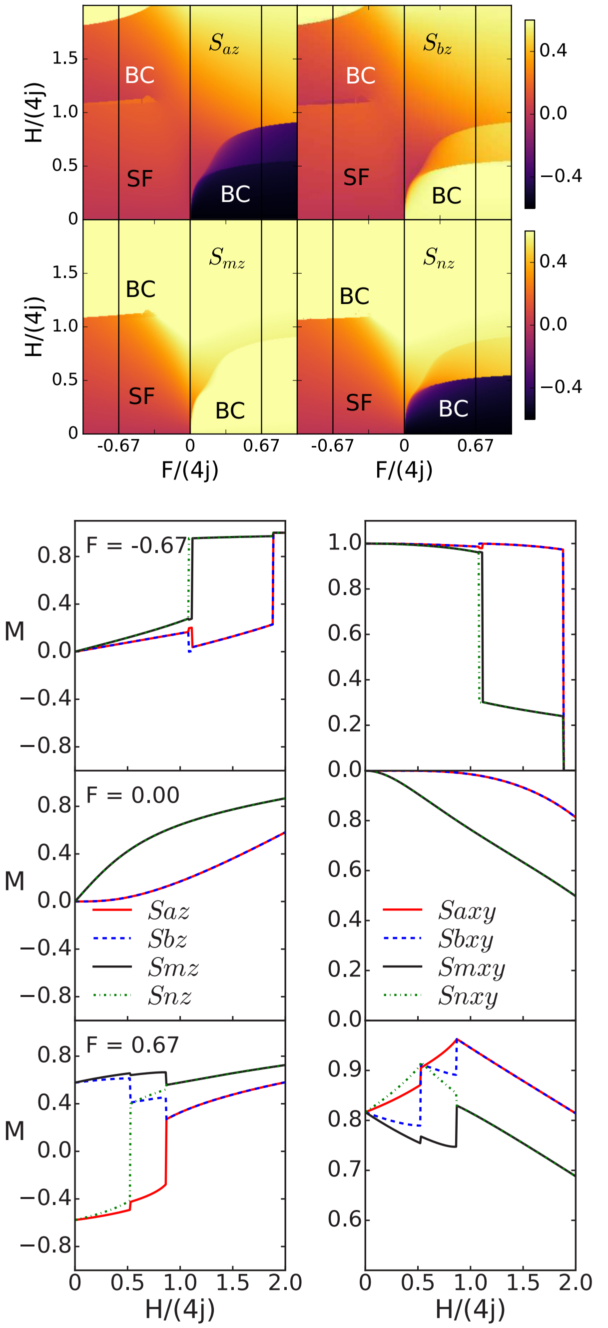

FIG. 10. The ground-state configuration for $J/(4j) = 2/3$ for the moments along H applied in the z direction for the four types of spin as a function of H and F (top) calculated by minimizing the energy in Eq. (2) and the moments of each component parallel (left) and perpendicular (right) of the spins as a function of H along cuts at $F/(4j) = -0.67$, 0, and 0.67 (bottom). Biconical states (BC) similar to those in Fig. 9 are observed as well as an intermediate state between the biconical state and the paramagnetic state for $F > 0$.

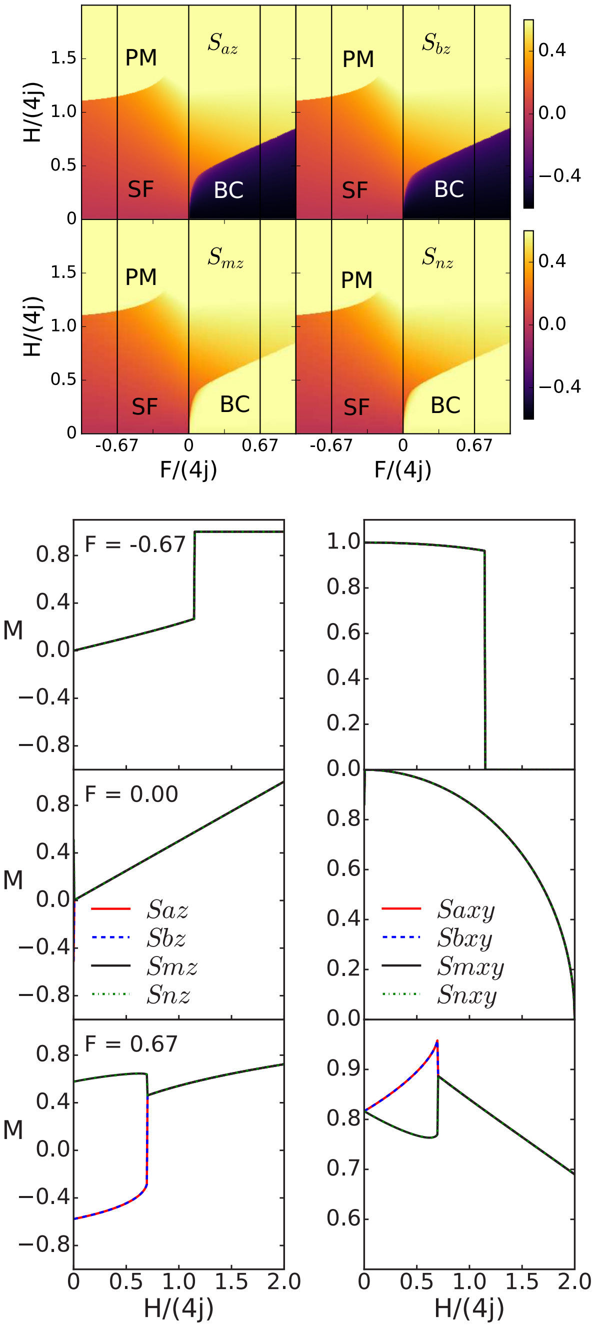

FIG. 11. The ground-state configuration for $J/(4j) = -2/3$ for the moments along H applied in the z direction for the four types of spin as a function of H and F (top) calculated by minimizing the energy in Eq. (2) and the moments of each component parallel (left) and perpendicular (right) of the spins as a function of H along cuts at $F/(4j) = -0.67$, 0 and -0.67 (bottom). A biconical state (BC) is observed for $F > 0$.

$-7.5°$ with respect to z. The direction of z is only important when considering the case of tilt and we set it perpendicular to the twin interface.

Some differences are seen in the ground state as a result of the octahedron tilt, as shown in Fig. 12. For $F < 0$, the SF state for low fields and the BC1 state at intermediate fields appear qualitatively similar to the case of no tilt in Fig. 10, except that, for high H values, instead of a transition from the SF state to the PM state seen in Fig. 10, a new BC1-like state exists between the SF and PM states with S_a and S_b nearly perpendicular to each other and with S_m and S_n nearly parallel. For $F > 0$, the tilt and no tilt ground states appear superficially similar, but the transition between PM and BC2 states are separated by an

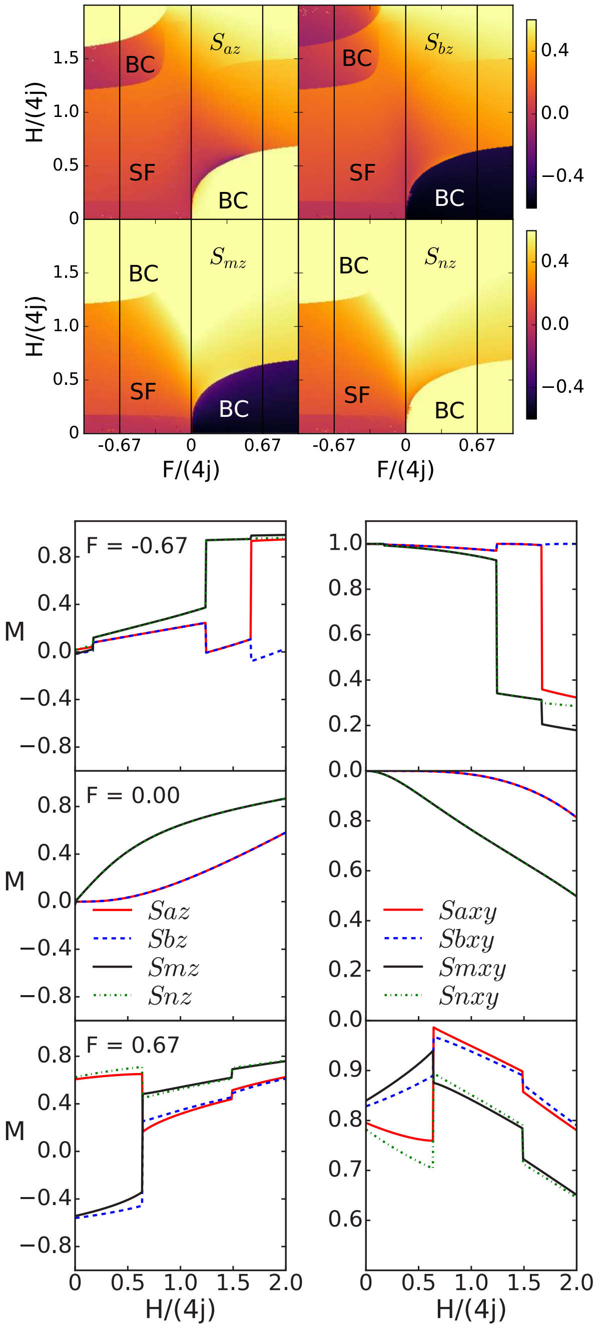

FIG. 12. The ground-state configuration with $J = J/(4j) = 2/3$, similar to that shown in Fig. 10 except that the oxygen octahedra are tilted with respect to z in an alternating pattern as described in the text. A biconical-like (BC) state is observed for both $F > 0$ and $F < 0$.

intermediate state as F increases. The transitions become less sharp as F decreases towards zero.

V. MEAN-FIELD APPROXIMATION

To study the model for $T > 0$, we employed the mean-field approximation

$$\mathcal{H} = \sum_{k\in a,b,m,n} \vec{S_k} \cdot \vec{H}_{\mathrm{MF},k}, \tag{5}$$

with the effective mean fields

$$\begin{aligned}
\vec{H}_{\mathrm{MF},a} &= 4j\overrightarrow{\langle S_m\rangle} + J\overrightarrow{\langle S_b\rangle} + \vec{H} + F\vec{C}_a,\\
\vec{H}_{\mathrm{MF},b} &= 4j\overrightarrow{\langle S_n\rangle} + J\overrightarrow{\langle S_a\rangle} + \vec{H} + F\vec{C}_b,\\
\vec{H}_{\mathrm{MF},m} &= 4j\overrightarrow{\langle S_m\rangle} + \vec{H} + F\vec{C}_m,\\
\vec{H}_{\mathrm{MF},n} &= 4j\overrightarrow{\langle S_b\rangle} + \vec{H} + F\vec{C}_n,
\end{aligned} \tag{6}$$

with the four terms

$$\vec{C}_p = \overrightarrow{\langle S_p\rangle} \odot \overrightarrow{\langle S_p\rangle} \odot \overrightarrow{\langle S_p\rangle}, \tag{7}$$

where $p = a, b, m,$ or n in each term. The exchange parameters j and J are those introduced earlier and summarized in Fig. 8. The symbol $\odot$ represents the Hadamard vector product; it is a piecewise multiplication of x, y, and z components yielding components such as $(S_{ax})^3$, $(S_{ay})^3$, $(S_{az})^3$ in the x, y, and z directions, respectively.

To calculate the total magnetization of each spin, we used the Helmholtz free energy $F = -T\ln Z_T$, with $Z_T = Z_a Z_b Z_m Z_n$, where

$$Z_k = \int \exp[-\beta\vec{S_k}\cdot\vec{H}_{\mathrm{MF},k}]\,d\Omega, \tag{8}$$

with $k = a, b, m,$ or n. The average moment for each spin is calculated using

$$\langle S_k\rangle_i = \frac{T}{Z_k}\frac{\partial Z_k}{\partial H_{\mathrm{MF},ki}}, \tag{9}$$

where $i \in x,y,z$ and $k \in a,b,m,n$.

To study the ZFC and FC temperature dependencies of the moments, we use the Levenberg-Marquardt (LM) algorithm [27], as described in Appendix. We increment the temperature to T_i and start the algorithm using the solution of the previous T_{i-1} as a seed.

In experiments, the FC and ZFC temperature scanning procedures were used. We will argue from the mean-field simulations that FC results in a metastable state, whereas ZFC creates a state closer to equilibrium.

The mean-field FC scans are started at high T and cooled in the field. In the second procedure, the simulation starts with the system in the equilibrium state at low T and is heated with H_z applied. This is similar to the experimental ZFC procedure in that the system starts from a state close to equilibrium. We will use the ZFC label for the mean-field procedure starting at low T in the equilibrium state.

For $J/(4j) = 2/3$, and $H_z/(4j) = 2.27 \times 10^{-4}$, we show typical results in Fig. 13 for average spin moments parallel (left) and perpendicular (right) to H_z versus T for $F/(4j) = -0.67$, 0, and 0.67 for both the FC and ZFC procedures. For this figure and all the other figures in this section, the temperature scale T is normalized so that the FC transition for $J/(4j) = 2/3$ is at $T_C = 89.5$ K, the experimentally observed transition temperature for the net moment. The ZFC transitions occur at $T = T_{\mathrm{eq}}$. The total moment along the magnetic field is $T_z = S_{az} + S_{bz} + S_{mz} + S_{nz}$ and total moment perpendicular to the field is $T_{xy} = \sqrt{\sum_{i\in x,y}(S_{ai} + S_{bi} + S_{mi} + S_{ni})^2}$. For $F/(4j) = -0.67$, the equal moments on S_m and S_n are aligned with H_z and the equal moments on S_a and S_b are smaller and aligned opposite to H_z. This configuration yields a significant net moment along H_z for $T < T_C$. Above T_C, the very small moments induced by H_z on S_m and S_n are larger than those

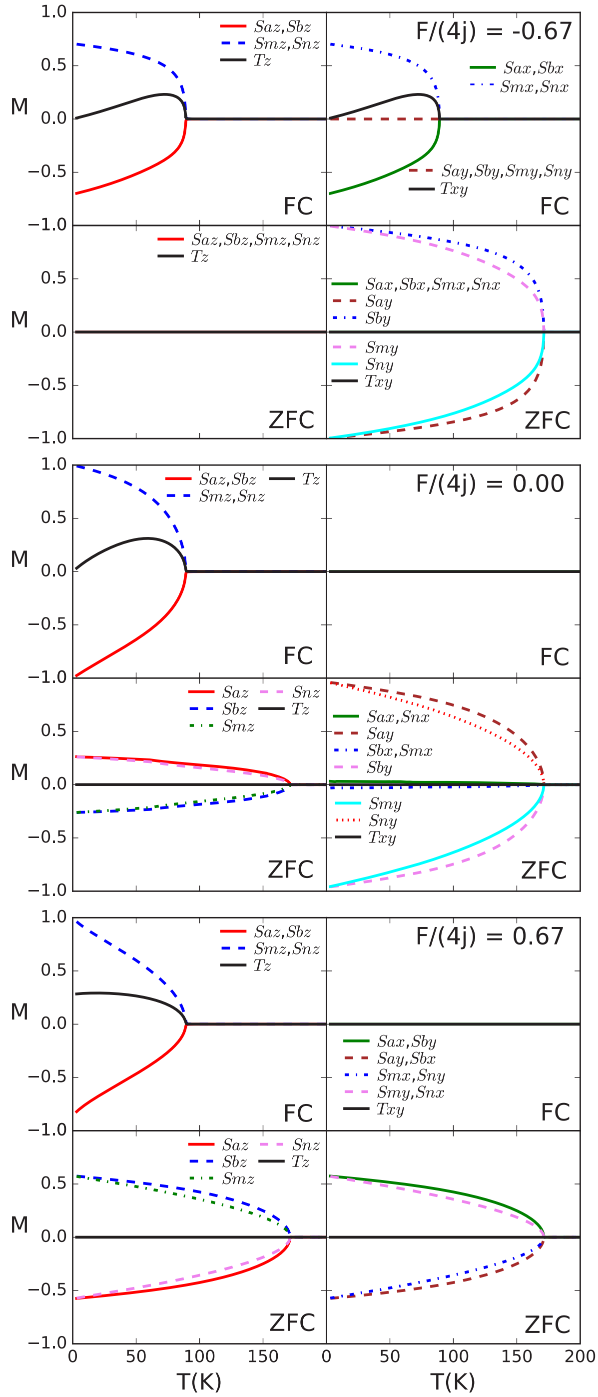

FIG. 13. The average moments of each spin component as well as the net moment T_z along H and T_{xy} perpendicular to H, where H is an applied field equivalent to $H_z = 20$ Oe for FC and ZFC with $J/(4j) = 2/3$ and $F/(4j) = -0.67$, 0, and 0.67. In the ZFC procedure, the system is started in its ground state at low temperature. All interactions are antiferromagnetic.

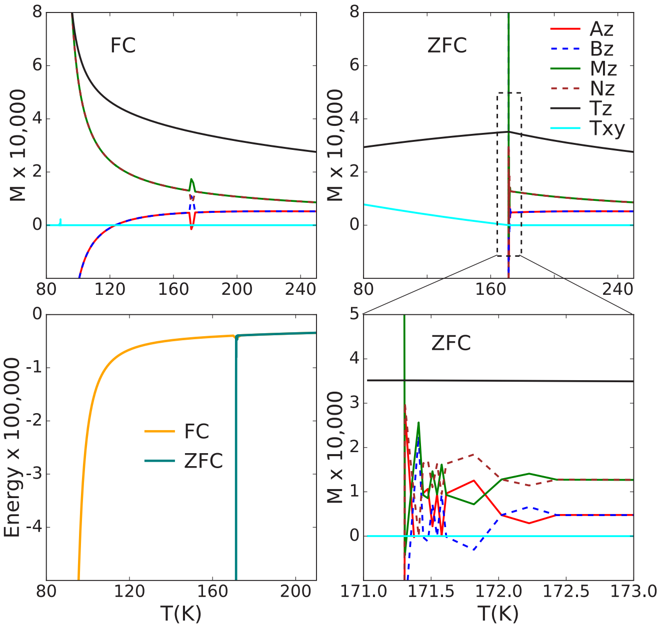

FIG. 14. The behavior of the moments near T_{eq} for $J/(4j) = 2/3$, showing the polarization of the sublattices for FC and ZFC as well as the energy for FC and ZFC. The smooth growth of the weak FC ferrimagnetic moment contrasts to sharp SF transition observed in ZFC.

on S_a and S_b and this preference for the alignment of S_m and S_n gets locked in below T_C, despite the energy cost of having S_a and S_b aligned. This is clearly a metastable state. If the system starts from the ground-state configuration, which is likely representing the ZFC state, S_a and S_b align in opposite directions, all spins align in an antiferromagnetic configuration, and no strong net moment develops.

For $F/(4j) = 0.67$, the FC behavior is similar for the net moment along H_z, but with a net moment growing more slowly below T_C and decreasing less at small T. The ZFC behavior, however, exhibits the BC2 state at low T, consistent with the ground-state calculation. The BC2 state has its transition at a higher temperature, $T_{\mathrm{eq}} \approx 170$ K, and it has no strong net moment parallel or perpendicular to H_z.

For $F = 0$, the FC behavior is intermediate between the $F/(4j) = -0.67$ and 0.67 cases, but the ZFC case shows a BC-type state with the higher transition temperature T_{eq}. Again, only FC shows a significant net moment along H_z. The metastable FC state is achieved when the LM algorithm settings suitably limit the explorable parameter space, as detailed in Appendix.

The mean-field simulation cannot answer the question of whether the real system will achieve the equilibrium state upon FC or enter the metastable state. We can equilibrate the system in the simulation upon FC if we allow each iteration in temperature to sample a large enough region of parameter space. On the other hand, we know that the real LCO system shows strong hysteresis; FC results in a significant net moment and ZFC produces a much reduced moment. This indicates that for FC, the LCO system has a difficult time transforming from the state above T_{eq} to the equilibrium state is entered upon ZFC. The simulation results near T_{eq} indicate why this might be. Figure 14 shows the two configurations of spin moments obtained upon FC and ZFC for the case $F/(4j) = 0.67$. For ZFC, the system retains antiferromagnetic order for all $T \leqslant T_{\mathrm{eq}}$, with S_b and S_m along H_z and S_a and S_n in the opposing direction. The four sublattice magnetizations nearly cancel for $T \leqslant T_{\rm eq}$, as they also do for $T \geqslant T_{\rm eq}$. Above $T_{\rm eq}$, the small net magnetization decreases as T increases and the moments on S_m and S_n are significantly larger than those of S_a and S_b.

The FC situation for $T > T_{\rm eq}$ is identical to the ZFC one. However, as T decreases below $T_{\rm eq}$, the system cannot easily transition to the ZFC state. On both sides of the twin interface, the sublattices with S_m and S_n are more polarized along the field than the S_a and S_b sublattices. In order to reach the ZFC state, the entire sublattices on one side of the interface must reverse direction. The antiferromagnetic interactions between S_a and S_b can help facilitate the reversal, but it is not easy to achieve the reversal through short-range fluctuations in the same way that a uniform antiferromagnet would. In the latter case, independent regions of antiferromagnetically correlated regions fluctuate and grow in size near the transition temperature; the fluctuating regions do not have to compete against a field-induced bias favoring the alignment of one sublattice with the field over the other. In the interface case, the spins with the largest moments, S_m and S_n, do not interact directly and the bias created by the field throughout the lattices on each side of the interface opposes equilibration of the entire system. If the system does not equilibrate close to $T_{\rm eq}$, it only becomes harder as T decreases because the field-induced bias of the sublattice moments increases. Although the field-induced bias at each site is small, the overall effect of the bias is strong because it permeates the entire system, effectively eliminating the ability of local fluctuations to reverse entire sublattices. Although S_a and S_b are not aligned, despite the antiferromagnetic interaction between them, the system orders at a temperature T_C, which is much lower than $T_{\rm eq}$.

Although the mean-field simulation cannot equilibrate through thermal fluctuations, upon each change in temperature we allow the system to vary the initial parameters within set limits. If these variations are allowed to be large enough, the ZFC state, which is closer to equilibrium, can be achieved upon FC. The variation of one parameter affects an entire sublattice; this facilitates the reversal of that entire sublattice at once, eliminating the need for local fluctuations to grow against the field-induced bias for the S_m and S_n sublattices to align with the field.

For $T < T_{\rm eq}$, the nonequilibrated FC system acts like a weak ferrimagnet with different moments on the two sublattices on either side of the interface. When T decreases to T_C, the system orders antiferromagnetically with the two unequal sublattice moments creating a net moment. Unlike the ZFC antiferromagnetic transition that remains sharp at $T_{\rm eq}$ independent of the magnitude of H, the ferrimagnetic-like transition rounds with increasing H because the field directly couples to the order parameter as a result of the unequal sublattice moments. If the real LCO system does not, in fact, readily achieve equilibrium, one could expect FC behavior like that observed in this model.

We also examined the case where $J/(4j) = -2/3$, shown in Fig. 15, where the ferromagnetic interaction favors the alignment of S_a and S_b in the same direction for both the FC and ZFC procedures. In this case, because there is no conflict caused by the field-induced larger moments on sublattices S_m and S_n and the ferromagnetic J, the transition temperatures T_C and $T_{\rm eq}$, for FC and ZFC, respectively, are nearly equal for all values of F. However, just as in the case for $J > 0$, H couples directly to the order parameter and the FC transition rounds rapidly as H increases. For ZFC, in contrast, the transition remains sharp as H increases. Unlike the $J > 0$ case, net moments occur for the ZFC case as well as for FC for $F \geqslant 0$ as a result of the unequal sublattice moments. Although the case $F < 0$ resembles the experiment, with a significant net moment only upon FC, the FC net moment decreases too rapidly

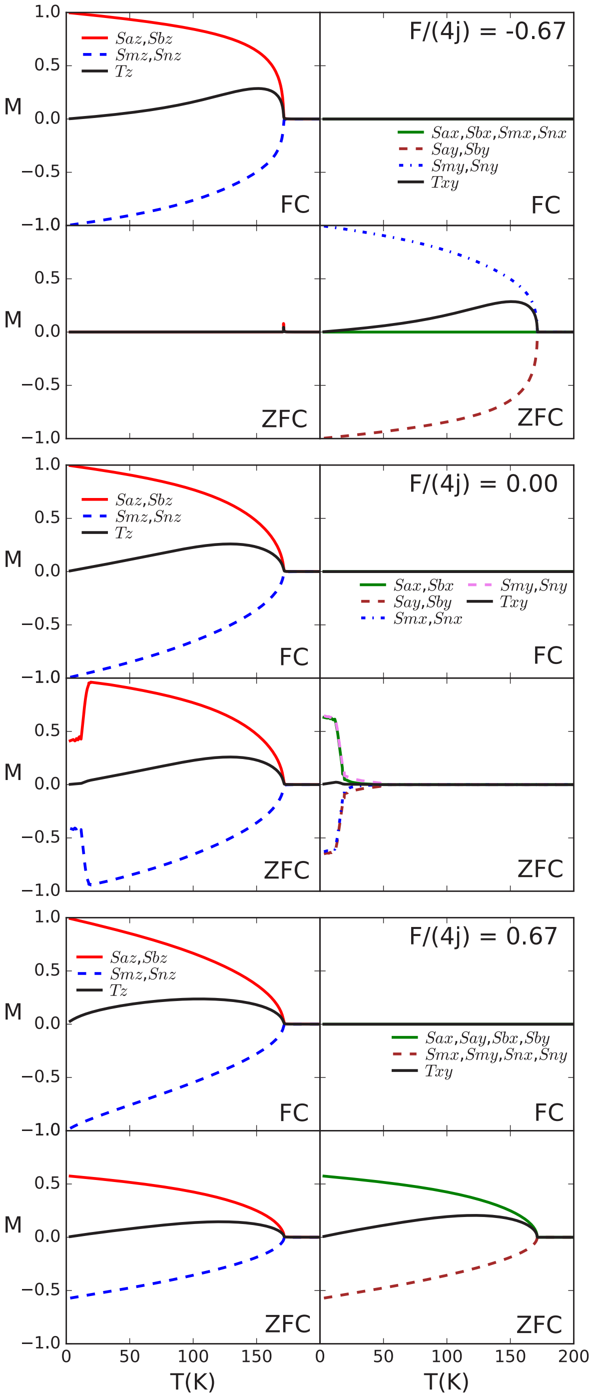

FIG. 15. The average moments of each spin component as well as the net moment T_z along H and T_{xy} perpendicular to H, where H is an applied field equivalent to $H_z = 20$ Oe for FC and ZFC with $J/(4j) = -2/3$ and $F/(4j) = -0.67$, 0, and 0.67. The interactions are all antiferromagnetic except between S_a and S_b which is ferromagnetic.

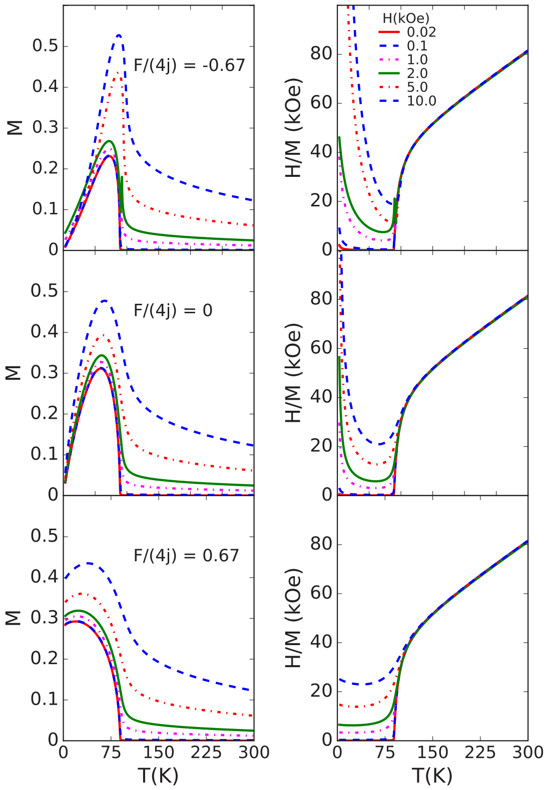

FIG. 16. The net moment M and H/M vs T upon FC for several fields with $J/(4j) = 2/3$ and $F/(4j) = -0.67$, 0, and 0.67.

with decreasing T to resemble the experiments. Because there is no reason to believe that the magnetic interaction is ferromagnetic for $\gamma = 165^\circ$ in LCO, we only compare $J > 0$ to the experimental magnetization data in the remaining part of this section.

The FC behaviors produced in the mean-field calculations for $J/(4j) = 2/3$ and all F resemble the net moment observed in the FC for magnetization experiments that measure the net moment along the field. The suppression of the moment in the magnetization experiments [2] upon cooling in very small fields, $H \leqslant 3$ Oe, is also consistent with the ZFC calculations that show no significant net moment. For the polarized neutron scattering experiments, the fields at the sample were $H_z \geqslant 16$ Oe, so the sample was in the metastable state for all the measurements.

Figure 16 shows the net moment along H_z and H_z/M versus T for various fields upon cooling for $J/(4j) = 2/3$. The field is normalized using the Curie law $M/H_z = C_m/T_m$ on an isolated spin with $g = 1$ and $S = 1$. The resulting conversion, $H_{\mathrm{kOe}} = 1.47H_z$, ensures that the field strengths reasonably reflect those used in the experiments. As H_z decreases, M versus T approaches an envelope below T_C that represents the spontaneous ordering. The transition is sharp near T_C for small H_z, but quickly rounds with increasing field. For H_z/M versus T, Curie-Weiss behavior is seen as a straight line above 150 K, and the net moment decreases H_z/M below T_C with rounding that increases rapidly for increasing H_z. This behavior mimics well that of the net moment observed in bulk LCO powders experiments, except that the experimental data include a large antiferromagnetic component from the bulk spins far from the interface that is not included in this model. Because the magnetization measurements [1,12] do not indicate a large decrease in the net moment as T decreases towards zero, the behavior for $F > 0$ most resembles the experimental results, though it must be remembered that the mean-field approximation suppresses the thermal fluctuations that exist in the LCO system.

Finally, we address the case where the oxygen octahedra are tilted in the configuration in the manner described in the previous section. Introducing the tilt, $\vec{C}_k$ take the form

$$\begin{aligned}
\overrightarrow{C}_a &= \mathbf{M_1}^{-1}[\mathbf{M_1}\overrightarrow{\langle S_a\rangle} \odot \mathbf{M_1}\overrightarrow{\langle S_a\rangle} \odot \mathbf{M_1}\overrightarrow{\langle S_a\rangle}],\\
\overrightarrow{C}_b &= \mathbf{M_2}^{-1}[\mathbf{M_2}\overrightarrow{\langle S_b\rangle} \odot \mathbf{M_2}\overrightarrow{\langle S_b\rangle} \odot \mathbf{M_2}\overrightarrow{\langle S_b\rangle}],\\
\overrightarrow{C}_m &= \mathbf{M_2}^{-1}[\mathbf{M_2}\overrightarrow{\langle S_m\rangle} \odot \mathbf{M_2}\overrightarrow{\langle S_m\rangle} \odot \mathbf{M_2}\overrightarrow{\langle S_m\rangle}],\\
\overrightarrow{C}_n &= \mathbf{M_1}^{-1}[\mathbf{M_1}\overrightarrow{\langle S_n\rangle} \odot \mathbf{M_1}\overrightarrow{\langle S_n\rangle} \odot \mathbf{M_1}\overrightarrow{\langle S_n\rangle}], \qquad (10)
\end{aligned}$$

where the appropriate rotation matrix expresses each spin vector in the coordinates of its respective oxygen octahedron, the Hadamard vector product is performed, and the resulting vector is then expressed in the original coordinate frame. Results from the ground-state $T = 0$ calculation using Eq. (10) are very close to those with finite T in Eq. (4), and the small T and H_z behavior from the mean-field calculation reflects the ground-state results. These results indicate that the effective mean field represented by Eq. (10) is a good indicator of the behavior when cubic isotropy is broken by the tilted octahedral geometry though it does not precisely reflect a cubic anisotropy in the coordinates of the octahedra. The results were not significantly different from the case of untilted octahedra, so we conclude that the tilt is not a dominant factor in the behavior of LCO magnetic behavior.

Although we have presented most results for a specific value $J/(4j) = 2/3$ and some results with $J/(4j) = -2/3$, we found qualitatively similar results for other values such as $J/(4j) = 4/3$ and $1/3$. The basic behavior does not seem sensitive to the magnitude of $J/(4j)$ chosen with $|J|$ comparable to, but larger than j.

For the model, we have shown that the net moment is generated by the twin interface. That result is not dependent on the sign of F or J, and tilting of the octahedra by the angle in LCO does not significantly alter behavior of the net moment. In the neutron scattering measurements, the observed scattering indicates components of the net moment perpendicular to the field. The top panel of Fig. 13 shows that, upon FC with $F < 0$, a perpendicular component is generated for the field aligned with an axis of the octahedron surrounding the Co ion. In an actual experiment, the field will not, in general, be aligned with one of the octahedral axes because the twin interfaces will be in many different orientations. For this reason, if $F > 0$, we would still expect a significant perpendicular component of the net moment with respect to the applied field because there will be a significant field component along all the octahedral axes. Only for $F = 0$, would there be no perpendicular component and only if the tilting is an insignificant factor.

VI. CONCLUSION

The mean-field calculation provides a plausible explanation for the observation of a significant net moment associated with critical-like behavior in LCO magnetization and neutron scattering experiments, its rapid rounding in relatively small fields, and the large difference in behavior for results obtained from the FC and ZFC procedures. The twin interface results in large interactions across the twin boundaries on half the sites with neighboring sites having no magnetic interaction. This asymmetry imposed on the sublattices enables a ferrimagnetic-like transition in the metastable state that rounds quickly with the field. One significant implication of the model is that LCO can exhibit a net moment in the absence of any ferromagnetic interaction between spins.

Critical fluctuations are suppressed in mean-field models, and more sophisticated techniques might modify the physical picture derived in the present model. However, the apparent consistency between the mean-field model and the experimental observations, particularly the large differences between the behavior in FC and ZFC, suggest that the model captures much of the essence of the physics, which is that the asymmetric influence of the twin interface on the two antiferromagnetic sublattices results in a FC metastable state with a significant net moment.

LCO surfaces have a larger average value of γ than the interior [7]. The resulting strain is likely accommodated by twinning. Similarly, strain near impurity defects can be released through high densities of twin interfaces. The large net moment observed in LCO with large strain or defects is likely attributable to the induced twinning. Understanding the physical mechanism behind the appearance of a net moment in LCO is important in the design of thin-film devices using this material [28,29] and systems with similar properties.

The model presented here is for the net moment that forms near $T = 89$ K at twin interfaces in LCO. It does not address the behavior of the bulk moments in LCO. In particular, interesting behavior takes place as the temperature decreases to $T \approx 40$ K where the bulk magnetic moment decreases precipitously [1,3]. At low temperatures, quantum-based models [30] and experimental interpretations [31,32] have been proposed for the formation of excitons and for exciton condensation.

ACKNOWLEDGMENTS

The authors thank Alice Durand, Brendan Wells, and Frank Bridges for helpful discussions. We also thank Qing Huang and Haidong Zhou for their efforts in growing crystals for the experiments. The calculations were done on the UCSC Hyades (NSF award AST-1229745) and Hummingbird computational clusters. Research at ORNL's HFIR was sponsored by the Scientific User Facilities Division, Office of Basic Energy Sciences, U.S. Department of Energy. J.-Q.Y. was supported by the U.S. Department of Energy, Office of Science, Basic Energy Sciences, Materials Sciences and Engineering Division.

APPENDIX

To find the ground state, we minimize Eqs. (2)–(4) using the algorithm SLSQP (Sequential Least SQuares Programming) from the SCIPY package [27]. It minimizes $\mathcal{H}$ subject to the constraints $\sqrt{S_{ix}^2 + S_{iy}^2 + S_{iz}^2} = 1$ with $i \in a,b,m,n$. Because SLSQP is a local minimizer, a combination of several initial seeds are necessary to avoid being trapped in local minima.

For the finite-temperature mean-field calculations, we use a root finding algorithm from the scipy.optimize package [27]. It solves the system of nonlinear equations in a least squares sense using a modification of the Levenberg-Marquardt algorithm as implemented in MINPACK [33]. Integrals in Eq. (8) are solved numerically. We use a combination of QAG adaptive integration and QAGP adaptive integration with known singular points for difficult regions; the algorithms [34] are implemented in the GNU scientific library [35].

The Levenberg-Marquardt (LM) attempts to minimize

$$S(\mathbf{x}) = \sum_{i=1}^{12} (x_i - f_i(\mathbf{x}))^2 \tag{A1}$$

for a given set of parameters. Equation (A1) is minimized with $x_i = \langle S_k \rangle_j$ for $k \in a,b,m,n$ and $j \in x,y,z$, with $f_i = (T/Z_k)(\partial Z_k/\partial H_{\mathrm{MF},kj})$, representing a total of 12 equations and 12 variables. To first order,

$$S(\mathbf{x} + \boldsymbol{\sigma}) = \sum_{i=1}^{12} (x_i - f_i(\mathbf{x}) - J_i \boldsymbol{\sigma})^2. \tag{A2}$$

The Jacobian $\mathbf{J}$ is calculated numerically. For this algorithm, two stopping criteria were set,

$$\frac{||\mathbf{D}(\mathbf{x}_k - \mathbf{x}_{k+1})||}{||\mathbf{D}(\mathbf{x}_{k+1})||} \leqslant \mathrm{XTOL}, \tag{A3}$$

where $\mathbf{D}$ is the diagonal matrix specifying the allowed scale of $\mathbf{x}$, and

$$\frac{||\mathbf{f}(\mathbf{x}_k)||}{||\mathbf{f}(\mathbf{x}_{k+1})||} \leqslant 1 + \mathrm{FTOL}. \tag{A4}$$

Here, k indicates the step of the algorithm. We set $\mathrm{XTOL} = \mathrm{FTOL} = 1.5 \times 10^{-8}$. Because LM finds only the local minimal, choosing the best initial $\mathbf{x}_0$ and $\mathbf{D}_0$ is paramount in determining whether the calculation finds the equilibrium or a metastable state. For ZFC, the SLSQP algorithm is used to find the global minimal state for $T = 0$. This state is then used as the initial $\mathbf{x}_0^0$ for the LM algorithm at finite T_0 for $T_0 > 0$. The scaling matrix is set to $\mathbf{D}_0^0 = |\mathbf{x}_0^0|$. The LM algorithm produces the value $\mathbf{x}_{\text{final}}^0$, which is the spin configuration at T_0 (the subscript "final" indicates the final result of k iterations). For each T_{q+1} calculation, the previous result at T_q is used as the seed. For FC, we start at high T and decrease the temperature on each iteration, i.e., $T_q < T_{q-1}$. For each T_q, the size of the initial step of LM algorithm is $\delta||\mathbf{D}_0^q \mathbf{x}_0^q||$ with $\delta = 1$ and $\mathbf{x}_0^q = \mathbf{x}_{\text{final}}^{q-1}$ is the spin configuration for previous T_{q-1}. The scaling matrix is $\mathbf{D}_0^q = |\mathbf{x}_0^q|$. Specifying $\mathbf{x}_0^q$ and $\mathbf{D}_0^q$ in this way constrains the parameter space so that the state is metastable, as observed in the LCO experiments. If the value of δ or minimal floor on $\mathbf{x}_0^q$ and $\mathbf{D}_0^q$ is increased, this results in a larger parameter space, corresponding to higher likelihood of finding the equilibrium state in FC.

[1] A. M. Durand, D. P. Belanger, C. H. Booth, F. Ye, S. Chi, J. A. Fernandez-Baca, and M. Bhat, J. Phys.: Condens. Matter **25**, 382203 (2013).
[2] A. M. Durand, T. J. Hamil, D. P. Belanger, S. Chi, F. Ye, J. A. Fernandez-Baca, Y. Abdollahian, and C. H. Booth, J. Phys.: Condens. Matter **27**, 126001 (2015).
[3] D. P. Belanger, T. Keiber, F. Bridges, A. M. Durand, A. Mehta, H. Zheng, J. F. Mitchell, and V. Borzenets, J. Phys.: Condens. Matter **28**, 025602 (2016).
[4] M. Itoh, M. Sugahara, I. Natori, and K. Motoya, J. Phys. Soc. Jpn. **64**, 3967 (1995).
[5] Y. Lee and B. N. Harmon, J. Appl. Phys. **113**, 17E145 (2013).
[6] J.-Q. Yan, J.-S. Zhou, and J. B. Goodenough, Phys. Rev. B **70**, 014402 (2004).
[7] A. M. Durand, D. P. Belanger, T. J. Hamil, F. Ye, S. Chi, J. A. Fernandez-Baca, C. H. Booth, Y. Abdollahian, and M. Bhat, J. Phys.: Condens. Matter **27**, 176003 (2015).
[8] G. Maris, Y. Ren, V. Volotchaev, C. Zobel, T. Lorenz, and T. T. M. Palstra, Phys. Rev. B **67**, 224423 (2003).
[9] P. Vullum, R. Holmestad, H. Lein, J. Mastin, M.-A. Einarsrud, and T. Grande, Adv. Mater. **19**, 4399 (2007).
[10] P. E. Vullum, H. L. Lein, M.-A. Einarsrud, T. Grande, and R. Holmestad, Philos. Mag. **88**, 1187 (2008).
[11] R. M. Moon, T. Riste, and W. C. Koehler, Phys. Rev. **181**, 920 (1969).
[12] J.-Q. Yan, J.-S. Zhou, and J. B. Goodenough, Phys. Rev. B **69**, 134409 (2004).
[13] K. Binder and P. C. Hohenberg, Phys. Rev. B **6**, 3461 (1972).
[14] K. Binder and P. C. Hohenberg, Phys. Rev. B **9**, 2194 (1974).
[15] K. Asai, P. Gehring, H. Chou, and G. Shirane, Phys. Rev. B **40**, 10982 (1989).
[16] D. Phelan, D. Louca, S. Rosenkranz, S.-H. Lee, Y. Qui, P. J. Chupas, R. Osborn, H. Zheng, J. F. Mitchell, J. R. D. Copley, J. L. Sarrao, and Y. Moritomo, Phys. Rev. Lett. **96**, 027201 (2006).
[17] A. Podlesnyak, S. Streule, J. Mesot, M. Medarde, E. Pomjakushina, K. Conder, A. Tanaka, M. W. Haverkort, and D. I. Khomskii, Phys. Rev. Lett. **97**, 247208 (2006).
[18] R. A. Cowley, M. Hagen, and D. P. Belanger, J. Phys. C **17**, 3763 (1984).
[19] D. Fuchs, L. Dieterle, E. Arac, R. Eder, P. Adelmann, V. Eyert, T. Kopp, R. Schneider, D. Gerthsen, and H. v. Löhneysen, Phys. Rev. B **79**, 024424 (2009).
[20] J. W. Freeland, J. X. Ma, and J. Shi, Appl. Phys. Lett. **93**, 212501 (2008).
[21] D. Fuchs, E. Arac, C. Pinta, S. Schuppler, R. Schneider, and H. v. Lohneysen, Phys. Rev. B **77**, 014434 (2008).
[22] A. Herklotz, A. D. Rata, L. Schultz, and K. Dorr, Phys. Rev. B **79**, 092409 (2009).
[23] A. Posadas, M. Berg, H. Seo, D. J. Smith, A. P. Kirk, D. Zhernokletov, R. M. Wallace, A. de Lozanne, and A. A. Demkov, Microelectron. Eng. **88**, 1444 (2011).
[24] G. Bannasch and W. Selke, Eur. Phys. J. B **69**, 439 (2009).
[25] T.-C. Dinh and R. Folk, arXiv:0907.1480.
[26] M. Dudzinski, J. Sznajd, and J. Zittartz, Eur. Phys. J. B **17**, 575 (2000).
[27] T. E. Oliphant, Comput. Sci. Eng. **9**, 10 (2007).
[28] W. S. Choi, K. T. Kang, H. Jeen, Z. Gai, and H. N. Lee, Curr. Appl. Phys. **17**, 722 (2017).
[29] C. Hu, K. W. Park, A. Posadas, J. L. Jordan-Sweet, A. A. Demkov, and E. T. Yu, J. Appl. Phys. **114**, 183909 (2013).
[30] J. F. Afonso and J. Kunes, Phys. Rev. B **95**, 115131 (2017).
[31] S. El-Khatib, D. Phelan, J. G. Barker, H. Zheng, J. F. Mitchell, and C. Leighton, Phys. Rev. B **92**, 060404 (2015).
[32] S. R. Giblin, I. Terry, D. Prabhakaran, A. T. Boothroyd, and C. Leighton, Phys. Rev. B **79**, 174410 (2009).
[33] J. J. Moré, B. S. Garbow, and K. E. Hillstrom, ANL-80-74, 1980.
[34] R. Piessens, E. de Doncker-Kapenga, C. W. Überhuber, and D. K. Kahaner, *QUADPACK: A Subroutine Package for Automatic Integration* (Springer Science and Business Media, Berlin, 2012), Vol. 1.
[35] M. Galassi, J. Davies, J. Theiler, B. Gough, G. Jungman, M. Booth, and F. Rossi, *GNU Scientific Library* (Lightning Source, 2003).